

Phase Change Materials-Based Bilayer Metasurfaces for Near-Infrared Photonic Routing

Chensheng Li, Shuo Du, Ruhao Pan, Xiaoyu Xiong, Zhiyang Tang, Ruixuan Zheng, Yunan Liu, Guangzhou Geng, Jingbo Sun, Changzhi Gu,* Haiming Guo,* and Junjie Li*

Photonic routing holds immense significance in the fields of photonic integrated circuits (PICs) for free-space optical linking. The emergence of programmable metasurfaces with powerful phase regulation capability provides a promising strategy for achieving designated wavefront modulation and thus photonic routing in the optical communication waveband. Here, a bilayer metasurfaces with four-level codable unit pixels, which realize controllable photonic routing in near-infrared (NIR) region is reported. The unit pixel of the metasurfaces consists of the underneath amorphous silicon (α -Si) nanofin and the upper $\text{Ge}_2\text{Sb}_2\text{Te}_5$ (GST) nano-antenna, which contribute to the cross-polarization generation and amplitude modulation of cross-polarization light, respectively. Each unit pixel can be designated with desired states, thus achieving on-demand non-volatile photonic routing for coherent NIR light. In particular, polarization conversion modulation of the tunable metasurfaces comprising identical unit cell with large cross-polarization switching ($\approx 55\%$) at ≈ 1550 nm is demonstrated. Moreover, the metasurfaces with coded unit pixels to realize designated photonic routing are prototyped. The metasurfaces with four-level programmability portend a new paradigm in NIR photonic routing for PICs.

1. Introduction

Photonic integrated circuits (PICs) are highly desirable for applications in emerging fields, including optical computing, optical neural networks, and quantum information processing.^[1–4] Specifically, PICs have been expected to overcome the von Neumann bottleneck by minimizing the information transfer latency between the memory and processor, providing unprecedented optical solutions for logical operations.^[5,6] In recent years, significant progress has been made in the development of on-chip PICs.^[1,2,7] On the other hand, achieving optical links among PICs is a foreseeable evolution for the practical application of PICs in the future, which is essential for functional integration, coordinated operation, optical communication, and computing efficiency improvement. In particular, photonic routing devices are indispensable in these links as they tailor wavefront and thus distribute optical telecommunication

signals to terminal PICs via designated paths in free space. While the research on photonic routing for PICs is relatively lacking and requires further advancement.

Fortunately, metasurfaces provide an extremely competitive route for the realization of photonic routing. Metasurfaces are planar artificial sub-wavelength structure arrays with tailored optical responses, possessing abilities to arbitrarily modulate the amplitude, phase, and polarization of the incident optical signal.^[8–11] Several types of metasurfaces have been demonstrated to achieve wavefront regulation, including light focusing, holographic imaging, polarization control, and beam steering.^[9,12–16] The adjustability of structure configuration in metasurfaces endows them with great flexibility for light-scattering behaviors. Notably, static metasurfaces possess limited wavefront manipulation abilities due to the fixed optical responses. Active tuning becomes unattainable once the static metasurfaces are being fabricated, which confines the potential application scenarios and restricts the extension of optical functions. In contrast, tunable metasurfaces are particularly significant and popular for their optical responses can be dynamically modulated, providing great convenience for distributing optical signals in on-demand manners.^[17–21] In particular, programmable metasurfaces have immensely high

C. Li, S. Du, R. Pan, Z. Tang, R. Zheng, Y. Liu, G. Geng, C. Gu, H. Guo, J. Li
Beijing National Laboratory for Condensed Matter Physics
Institute of Physics
Chinese Academy of Sciences
Beijing 100190, China
E-mail: czgu@iphy.ac.cn; hmguo@iphy.ac.cn; jjli@iphy.ac.cn

C. Li, S. Du, R. Zheng, C. Gu, H. Guo, J. Li
CAS Key Laboratory of Vacuum Physics
School of Physical Sciences
University of Chinese Academy of Sciences
Beijing 100049, China

S. Du
BOE Technology Group Co.
Ltd.
Beijing 100176, China

X. Xiong, J. Sun
State Key Laboratory of New Ceramics and Fine Processing
School of Materials Science and Engineering
Tsinghua University
Beijing 100084, China

J. Li
Songsan Lake Materials Laboratory
Dongguan 523808, China

 The ORCID identification number(s) for the author(s) of this article can be found under <https://doi.org/10.1002/adfm.202310626>

DOI: 10.1002/adfm.202310626

degree of freedom in wavefront routing owing to the tunability of each unit pixel.^[22] Several strategies have been demonstrated to achieve programmable metasurfaces in microwave and terahertz regions, including diode, liquid crystal, varactor, and polarization tuning switch.^[22–25] It is worth mentioning that the optical telecommunication window at 1550 nm is widely adapted in the operation of PICs. Thus, achieving wireless route guidance in free space relies on the powerful wavefront manipulation capacity of the near-infrared (NIR) programmable metasurfaces. Recently, programmable metasurfaces for independent phase-amplitude control and non-volatile phase-only modulation of spatial light in NIR region have been demonstrated.^[26,27] These studies yield highly meaningful results and enlighten novel programmable schemes. On that basis, investigating metasurfaces with controllable unit pixels operating in the NIR region for photonic routing possesses extremely promising prospects.

Ge₂Sb₂Te₃ (GST) is one of the well-established phase-change materials with wide applications in optical disk memory.^[28] The transition of GST from an amorphous to crystalline state causes a significant change in its optical parameters in the visible and infrared region, which originates from the increase of delocalized bonding electrons,^[29,30] resulting in a corresponding high-contrast optical performance. On that basis, several strategies for tunable GST metasurfaces working in the NIR region have been proposed and yield excellent results.^[31–33] In addition, GST-based on-chip optical devices have been exploited as NIR photonic switches and memories for PICs, demonstrating the feasibility of GST applications in PICs.^[34–36] Therefore, it is excellent to leverage GST-based programmable metasurfaces to realizing NIR photonic routing due to the perfect compatibilities of both working waveband and phase transition tuning. Besides, the phase transition of GST is non-volatile and external excitation supply is needless after the phase change, which avoids static power consumption in enduring wavefront modulation.

In this work, we proposed and experimentally demonstrated a bilayer transmissive metasurfaces with four-level unit pixels, which realize on-demand photonic routing in NIR region. The all-dielectric double-layer nanostructure cell comprising upper GST nano-antenna and bottom amorphous silicon (α -Si) nanofin is adopted as the unit pixel for Pancharatnam-Berry (PB) phase modulation, which strongly diminish the unnecessary transmission loss compared with metallic counterpart. The α -Si nanofins and GST nano-antennas contribute to cross-polarization generation and amplitude modulation of cross-polarization light, respectively. To verify the cross-polarization modulation, we first fabricated tunable metasurfaces with same unit cell orientation. The cross-polarization transmissivity is $\approx 76.1\%$ for the tunable metasurfaces in amorphous state. The absolute polarization conversion variation (PCV) induced by GST phase change is $\approx 55\%$ at 1550 nm, showing large polarization conversion modulation depth. On that basis, the metasurfaces constituted by arranged four-level phase unit pixels is proposed. Each unit pixel is expected to be independently controlled by pulsed laser, which would greatly satisfy the need of on-demand non-volatile wavefront modulation and thus photonic routing. Then, we demonstrated the scheme by fabricating metasurfaces with coded unit pixels to realize desired photonic transport. Our results provide a fully new path to control coherent light transmission with large modulation flexibility and exhibit promising opportunities for

programmable metasurfaces being applied in photonic routing devices.

2. Device Design and Working Principle

Figure 1a,b depicts the schematic diagrams of the tunable metasurfaces for polarization conversion switching, which comprising periodically arranged nanofins with accordant orientation. The polarization conversion efficiency (PCE) of the metasurface is high when GST components are in amorphous state, allowing transmission of most cross-polarized light at desired wavelength and thus the polarization conversion switch is “on”. In stark contrast, for GST in crystalline state, the corresponding PCE is low with most transmitted cross-polarized light being impeded. Consequently, the polarization conversion state of the metasurface is “off”. To achieve the ideal metasurface with polarization conversion modulation, a double-layer design is adopted with one layer contribute to high PCE and the other responsible for extremely sharp modulation of optical response. The detailed configuration of the unit cell is shown in Figure 1c. Quartz substrate is chosen for its high optical transmittance in NIR region, which provides convenience for transmissive scheme. Benefitting from its large refractive index n and small extinction coefficient k in NIR region (Figure S1, Supporting Information), sub-wavelength α -Si nanostructures could generate remarkably high-efficient optical modulation with low intrinsic loss. Thus, the anisotropic cuboid α -Si nanofins with different lengths of axes are located above the substrate to provide a phase difference between two orthogonally polarized wave components of transmitted light in an ultrashort distance. Notably, realization of tunable optical function requires the participation of reconfigurable factors. To reach this goal, GST nano-antenna with phase change attributes is introduced and covered on the top of α -Si nanofin. The dramatic modulation of PCE is therefore achieved. The lengths of long and short axes of the nanofin are $L = 600$ nm and $W = 200$ nm. The period of unit cells along x -axis and y -axis is $P = 580$ nm, and the heights of GST nano-antenna and α -Si nanofin are labeled as H_1 and H_2 , respectively. The orientation of the GST/ α -Si nanofin is characterized with clockwise rotation angle θ (Figure 1c), by changing which the extra PB phase delay would generate. The Poincare sphere in Figure 1d visually exhibits the PB phase generated in polarization conversion from right-handed circularly polarized (RCP) light to left-handed circularly polarized (LCP) light. Specifically, the PB phase φ_{PB} can be expressed as:

$$\varphi_{PB} = \frac{\sigma\Omega}{2} = 2\sigma\Delta\theta \quad (1)$$

where $\sigma = \pm 1$ denotes the states circular polarization, $\Delta\theta$ represents the related rotation angle, and Ω expresses the corresponding solid angle. The Equation (1) clearly shows that the extra PB phase φ_{PB} is twice as the relative rotation angle $\Delta\theta$. The Strehl ratio (SR) of a lens with n discrete phase levels can be represented as:

$$SR = \left[\left(\frac{n}{\pi} \right) \sin \left(\frac{\pi}{n} \right) \right]^2 \quad (2)$$

which is defined as the zero-order diffraction peak intensity normalized to that of the Airy disk. Large SR means high proportion

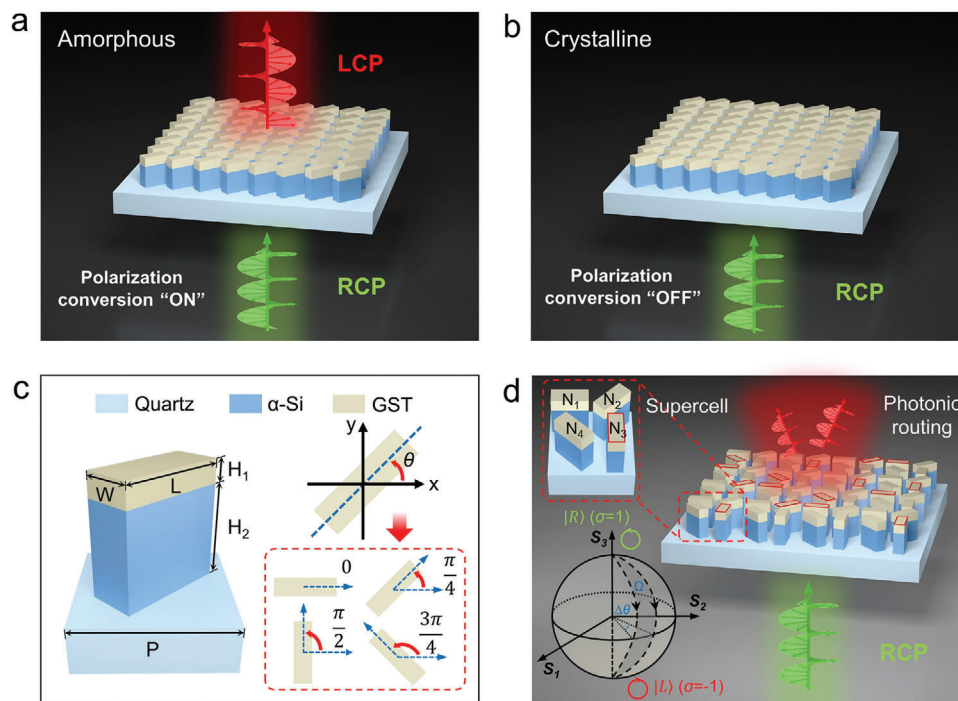


Figure 1. Schematic diagrams of the designed metasurfaces based on GST. Schematics of all-dielectric tunable metasurfaces for polarization conversion switching. The tunable metasurfaces exhibit polarization conversion of incident circularly polarized light in the “on” a) and “off” b) states, corresponding to the amorphous and crystalline states of GST, respectively. c) Schematic illustration of a unit cell of the metasurfaces with defined structure parameters and a clockwise rotation angle of θ . d) Schematic of programmed metasurfaces for NIR photonic routing. The metasurfaces are periodic arrays of supercells that comprise four nanofins (N_1 , N_2 , N_3 , and N_4) with specific orientation angles (0 , $\pi/4$, $\pi/2$, and $3\pi/4$). The GST nano-antennas of red frame-labeled nanofins are in amorphous states while the unlabeled counterparts denote crystalline ones. Poincare sphere in left bottom shows extra PB phase delays generated in polarization conversion of circularly polarized light.

of the main diffraction order for a phase modulation system. The SR is calculated as 81.1% for a four-level phase discretization, as shown in Figure S2 (Supporting Information), which will result in a satisfactory diffraction efficiency of wavefront control and suppression of high-order diffraction.^[37,38] Therefore, four discrete levels of PB phase (0 , $\pi/2$, π , and $3\pi/2$) covering the full 2π phase delay are respectively imparted by four nanofins (N_1 , N_2 , N_3 , and N_4) with different rotation angles (0 , $\pi/4$, $\pi/2$, and $3\pi/4$). In addition, the four nanofins (N_1 – N_4) together constitute a supercell, which further compose the metasurface in periodically arranged manner (Figure S3, Supporting Information). For the metasurface wholly in amorphous state (i.e., unprogrammed state), the cross-polarized transmission light is eliminated due to the destructive interference between the adjacent diagonal unit cells with π phase difference and equal transmission amplitude (between N_1 and N_3 , N_2 and N_4 , respectively). By crystallizing the three given GST nano-antennas in a supercell (without red frames), whose cross-polarized transmission amplitudes sharply diminish, the destructive interference balance between the remaining unit cell in amorphous state and the opposite one is broken, leading to the output of cross-polarized light through one supercell with large intensity and the same PB phase delay as the amorphous unit cell. The above crystallization operation to generate phase profile is identified as programming process, which is expected to be achieved by nanosecond pulsed laser. After the programming operation, the metasurfaces function as wireless optical signal-radiation devices for the incident NIR light.

The optical telecommunication signal that comes from the PICs can be guided to other PICs for optical linking. On that basis, a programmed metasurface with designed phase distribution is employed to yield wavefront routing.

3. Results and Discussion

3.1. Simulation Results of Designed Devices

The numerical simulation processes were performed using FDTD method. Detailed parameter settings used in the calculations are listed in the Experimental Section. We first employ α -Si nanofins to realize cross-polarization modulation, which is frequently utilized in metalens.^[39] The simulated transmission spectra of the metasurface comprising α -Si nanofins is illustrated in Figure 2a, where the structure parameters are set with height equals to 800 nm as well as $L = 600$ nm, $W = 200$ nm, and $P = 580$ nm. The cross-polarization and co-polarization transmissivity of the metasurface at 1550 nm are respectively 94.8% and 1.4%, demonstrating the extremely high polarization conversion efficiency at designed wavelength. To gain actively tunable ability, GST with changeable optical parameter is introduced (Figure 2b). As we can see, in NIR region, there are significant disparities between the refractive index n and extinction coefficient k of GST, making it suitable for realizing tailored optical modulation. Therefore, the top portion of the α -Si nanofin is intentionally replaced with GST to construct a GST/ α -Si nanofin (Figure 2c).

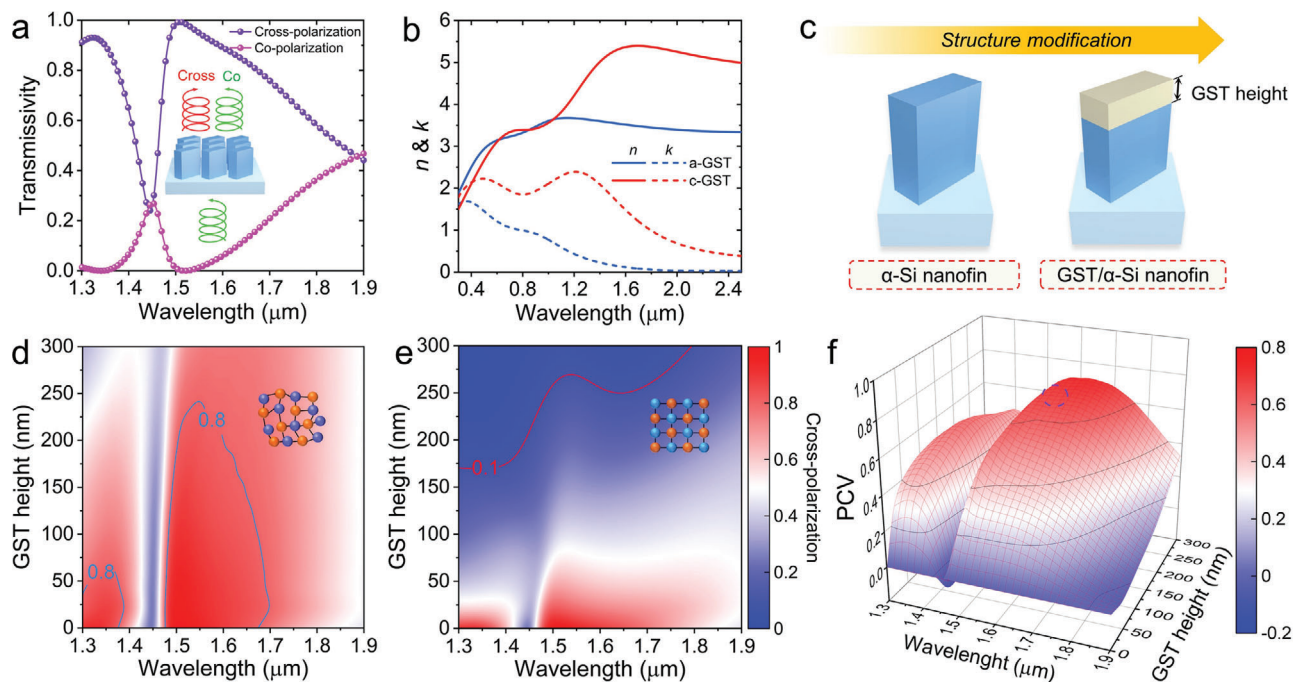


Figure 2. Configuration optimization of unit cells. a) Simulated transmission spectra of co- and cross-polarized light of α -Si metasurface (shown in the inset). b) Wavelength dependence of refractive index n and extinction coefficient k for GST. c) Structure modification of the unit cell from α -Si to GST/ α -Si nanofin. Simulated cross-polarization transmissivities versus GST height and wavelength for the tunable metasurfaces with GST in amorphous d) and crystalline e) states. f) Simulated PCV versus GST height and wavelength for the tunable metasurfaces. The appropriate height of the GST nano-antenna in GST/ α -Si nanofin for high PCV around the wavelength of 1550 nm is identified by the blue dotted circle.

To identify the optimal GST height, the cross-polarization spectra with varying GST height for both amorphous and crystalline states of the metasurfaces are simulated (Figure 2d,e). For the former, the cross-polarization efficiency decreases slowly with the increase of GST height around 1550 nm. The cross-polarization transmissivity maintains nearly 80% at ≈ 250 nm GST height, which remains a high-level of efficiency. While for the latter, the decline of the cross-polarization efficiency is obviously severe, especially at the beginning stage of GST height increasing. As the height of GST increases to ≈ 270 nm, the transmissivity decreases to ≈ 0.1 around 1550 nm. Besides, the $PCV = T_{cross}^{am} - T_{cross}^{cry}$ is calculated to characterize the absolute difference of the cross-polarization transmissivity between amorphous (T_{cross}^{am}) and crystalline (T_{cross}^{cry}) states. The simulated PCV versus GST height and wavelength are displayed in Figure 2f. With GST height increasing, the PCV increases quickly around 1550 nm in the initial stage due to the rapid decline of T_{cross}^{cry} . Then, the increasing trend decelerates and the PCV becomes leveling off. Consequently, the appropriate height of GST nano-antenna to achieve high PCV around 1550 nm is determined to be ≈ 250 nm and labeled by blue dotted circle (Figure 2f). To be specific, GST nano-antenna with 250 nm height is chosen for further analysis and sample fabrication, and the height of α -Si nanofin is thus set as 550 nm. Moreover, we also calculate the polarization conversation contrast (PCC) to quantify the switch ratio as a reference (Figure S4, Supporting Information), further revealing a giant modulation for cross-polarized light intensity. For the integrity of the structure parameters simulation, the transmissive cross-polarization spectra with period of the unit cell ranging from 580 nm to 650 nm

are given in Figure S5 (Supporting Information), which indicate that the change in the period has a minimal impact on the PCE.

Since the configuration of the unit cell with optimized structure parameters is identified, further targeted analyses are necessary for the tunable metasurfaces before experimental fabrication. Figure 3a depicts the simulation setup adopted in the numerical calculation processes. The total transmission spectrum for the metasurface in amorphous state is shown in Figure 3b, where the transmission around 1550 nm is $\approx 80\%$. In contrast, the transmission for the c-GST metasurface exhibits a significant decline, with the value at around 1550 nm dropping to only $\approx 17.7\%$ (Figure 3c). To explore the underlying mechanism, we analyzed electric field distribution profiles along long and short axis of the unit cells for both states (the insets in Figure 3b,c). It is obvious that the electric field intensity inside the a-GST nano-antenna is larger than that in the c-GST for both directions, which originates from lower extinction coefficient (Figure 2b) and thus lower optical loss of a-GST compared with c-GST. The cross- and co-polarization transmission spectra for amorphous GST metasurface are shown in Figure 3d, from which we could see that the cross-polarization component is the primary contributor to light transmission. Moreover, at the wavelength of 1550 nm, the cross-polarization transmissivity is about 79.5%, while the co-polarization transmissivity is only about 0.5%. The corresponding cross-polarization and co-polarization transmissivities at 1550 nm are 12.8% and 4.9%, respectively. To quantitatively exhibit the difference in cross-polarization efficiency induced by GST phase change, the wavelength-dependent PCV is calculated and exhibited in Figure 3f, which is identified as

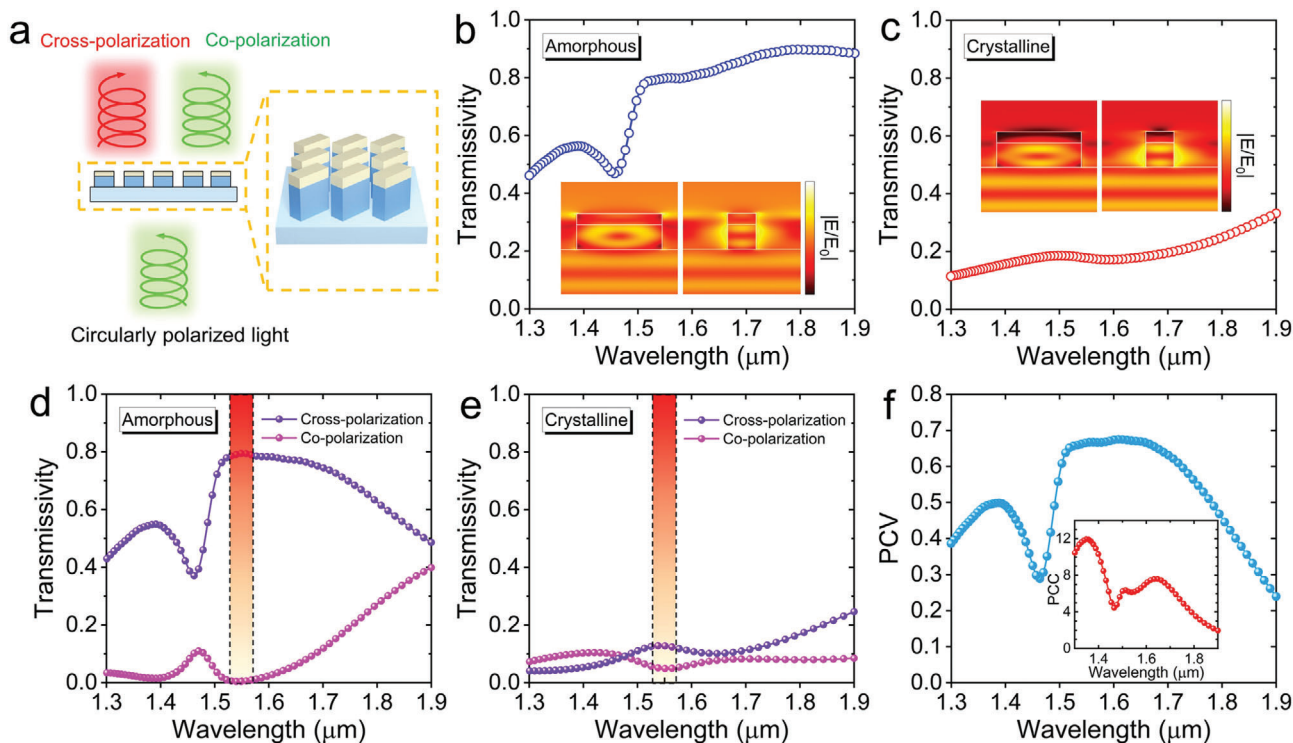


Figure 3. Simulated transmission spectra and electrical field analysis of tunable metasurfaces. a) Simulation schematic of the tunable metasurface for co- and cross-polarization transmission with circularly polarized light incidence. Wavelength dependence of total transmissivity for metasurfaces with a-GST b) and c-GST c). The insets exhibit electric field distribution profiles along long and short axis of GST/ α -Si nanofins. The cross- and co-polarization components of the total transmissivity versus wavelength for metasurfaces with a-GST d) and c-GST e). The spectrum range from 1530 nm to 1570 nm is indicated. f) Wavelength dependence of PCV that originated from phase transition of the metasurfaces. The inset illustrates wavelength-dependent PCC for the metasurfaces.

$\approx 66.7\%$ at 1550 nm. Such significant modulation depth of cross-polarization light is impressive for an all-dielectric transmissive-type scheme. The PCC versus wavelength is simulated to evaluate the optical response contrast from another point of view. The simulated result is presented in the inset of Figure 3f, with a PCC value of ≈ 6.2 at the wavelength of 1550 nm.

3.2. Fabrication and Measurement Results

Given the highly satisfactory simulation results, the following sections will present experimental results that further demonstrate our findings. Prior to device fabrication, the GST films were first characterized with several detection methods. Figure 4a illustrates the Raman spectra for both the amorphous and crystalline states of the GST films, with peaks at $\approx 152\text{ cm}^{-1}$ and 108 cm^{-1} serving as signatures of the two states, respectively. The Raman spectra of a-GST exhibit a peak that is broader than the one observed for c-GST. These results are consistent with previous reports.^[31,40] Figure S6 (Supporting Information) displays the X-ray diffraction (XRD) patterns, revealing the presence of Bragg peaks in c-GST and confirming its face-centered cubic (FCC) crystal structure. Moreover, atomic force microscope (AFM) and energy-dispersive X-ray spectrometer (EDS) are employed in turn to measure the roughness and element ratios of the GST films. The measured results are presented in Figures S7 and S8 (Sup-

porting Information), indicating a flat surface as well as uniform and accurate element composition. The detailed fabrication information is outlined in the Methods section, and the corresponding schematic diagram is depicted in Figure S9 (Supporting Information). During the fabrication process, HBr was selected as the etching gas for its high etching rate for both GST and α -Si as well as its comparatively minor etching damage to the GST components.^[41,42] SiO_2 hard mask is chosen due to the high selection ratio and slight impact on the metasurface performance even in the event of its non-removal.^[42,43] Figure 4b,c illustrates the scanning electron microscope (SEM) images of the as-fabricated metasurfaces, where excellent uniformity of the unit cell proves the effectiveness of the developed fabrication process. Due to the varied etching resistance of GST and α -Si, the transverse dimensions of GST and α -Si nanostructures are slightly different. The experimental transmission spectra for metasurfaces in amorphous and crystalline states are displayed in Figure 4d,e, respectively. The measured cross-polarization transmissivity around the 1550 nm wavelength range (1530–1570 nm) for the former exhibits a significantly higher value than the latter, which shows consistent trend with the simulation results. To elaborate, the cross-polarization transmissivities of the amorphous GST metasurface at 1530, 1550, and 1570 nm are $\approx 77\%$, 76.1% , and 72.8% , respectively (as shown in the inset of Figure 4e). In contrast, the corresponding values for the crystalline metasurface are $\approx 19.7\%$, 21.2% , and 20.8% . As a result, the polarization

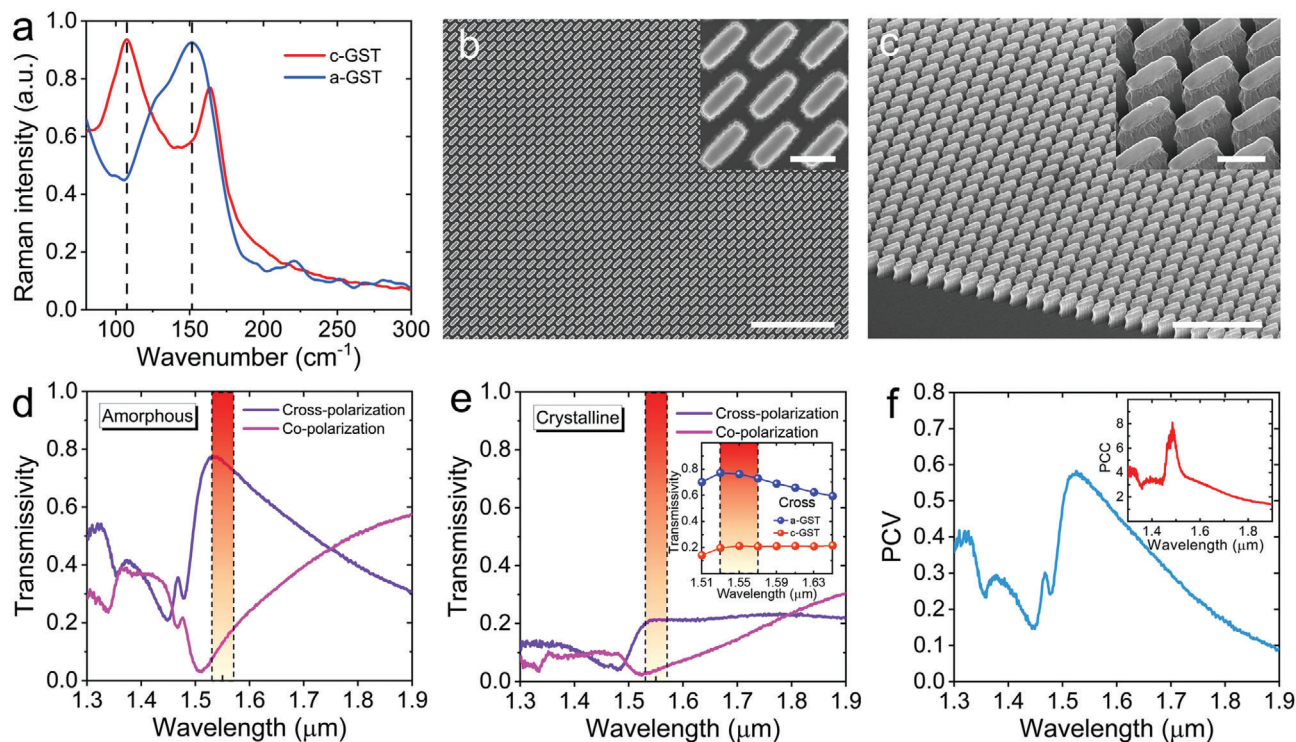


Figure 4. Experimental results of tunable metasurfaces fabrication and spectra measurement. a) Raman scattering spectra of a-GST and c-GST films growing on Si substrates. Top b) and titled c) view SEM images of the as-fabricated tunable metasurfaces. The insets show partial detailed SEM images of the unit cell. The scale bars in (b) and (c) are 5 and 3 μm, respectively, and both scale bars in the insets are 500 nm. Measured cross- and co-polarization transmission spectra for tunable metasurface with a-GST d) and c-GST e). The spectrum range from 1530 to 1570 nm is labeled. f) Wavelength dependence of PCV of the tunable metasurfaces. The inset displays measured results of wavelength-dependent PCC for metasurfaces.

conversion switching with both transmissive cross-polarization effect and bistable optical intensity control of cross-polarization light is experimentally realized. The deviation between simulated and experimental transmission spectra is mainly attributed to errors in the sample fabrication processes. Furthermore, the polarization conversion difference maintains at a wide spectral range of 1510–1650 nm, showing a broadband inclusiveness (inset of Figure 4e). The wavelength-dependent PCV is shown in Figure 4f, with the value of $\approx 54.9\%$ at 1550 nm and a maximum of $\approx 57.6\%$ at 1523 nm, demonstrating a significant modulation depth for polarization conversion efficiency. The PCC of the metasurface is ≈ 3.6 at 1550 nm and ≈ 8.1 at 1485 nm, which exhibit large switch ratio and further suggest the cross-polarization efficiency contrast induced by GST phase transition.

The tunable metasurfaces provide an innovative scheme for cross-polarization switching. On that basis, we also proposed and experimentally demonstrated a unique strategy to achieve metasurfaces with four-level programmability for photonic routing. Figure 5a shows the basic four-level nanofin unit cells with designed orientation angles which covering PB phase delay from 0 to 2π . The rotation angle difference $|\Delta\theta|$ of $\pi/4$ exists between adjacent levels, leading to a related PB phase delay of $\pi/2$. In addition, the four distinct cross-polarization paths are displayed in Poincare sphere in Figure 5a, along which the incident RCP light converts to LCP light. Each path corresponds to the cross-polarization modulation effect of a nanofin, which occurs when RCP light is transmitted through a nanofin unit.

The four nanofins with discrete phase levels are artificially arranged to constitute a supercell, which further forms the metasurface through periodic arrangement. For the circumstance that all the nanofins in amorphous state (i.e., unprogrammed state), the cross-polarized transmission light destructively interferes between the adjacent diagonal unit cells with π phase difference and equal transmission amplitude. As a result, there exists no wavefront modulation effect, which leads to the absence of photonic routing capability (Figure S10, Supporting Information). Moreover, one designated nanofin unit in each supercell is in amorphous state, while the other three units are set in crystalline state (Figure 1c). This operation is identified as programming process, which can be achieved by using a pulsed laser to selectively heat the specific area to induce GST crystallization. By this way, a programmed metasurface with desired wavefront modulation ability for photonic routing at 1550 nm is accomplished. The detailed steps for phase computation and metasurfaces programming are illustrated in Figure 5b. First, destinations of the transmissive cross-polarization light are arranged on the basis of photonic routing requirements. Following that, the phase distribution profiles for wavefront manipulation are obtained through numerical computation. The Experimental Section contains detailed information regarding the numerical computation process. Then, we employ a homemade algorithm for programming computation, which yields the corresponding coding distributions. Moreover, the metasurfaces are programmed with free-space laser according to the coding information. Meanwhile, the numerical

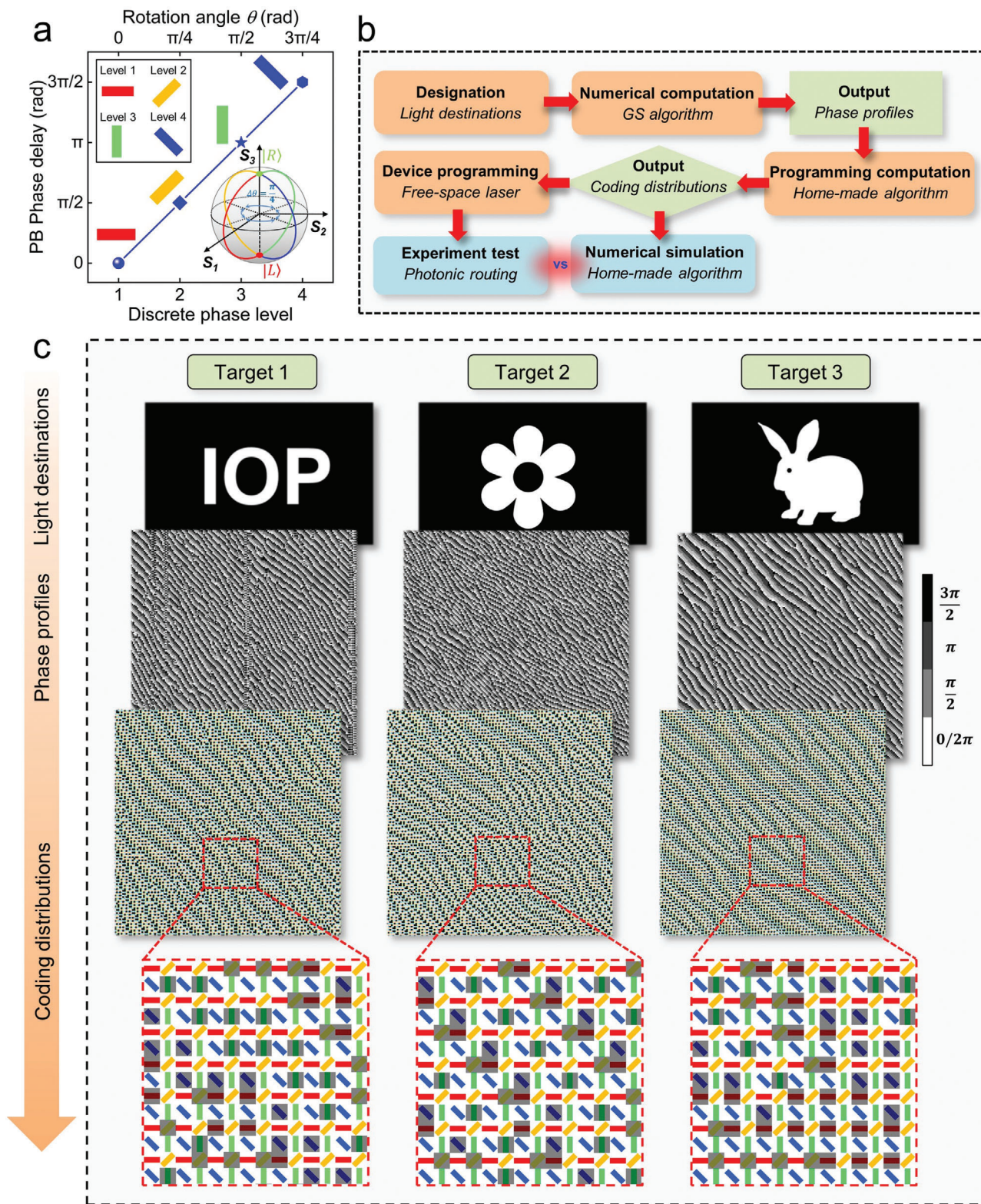


Figure 5. Schemes for photonic routing of the metasurfaces. a) PB phase delays generated from four discrete phase levels of nanofin units with diverse rotation angles. Poincare sphere in right bottom illustrates four corresponding paths in polarization conversion of circularly polarized light. b) Schematic diagram illustrating the detailed steps in phase computation and metasurfaces programming for photonic routing. c) Designated photonic routing targets associated with the corresponding four-level discrete phase profiles and coding distributions. The enlarged coding distributions are shown in the bottom panels, where the GST in nanofins selected by dark rectangles are in amorphous states and the others are in crystalline states.

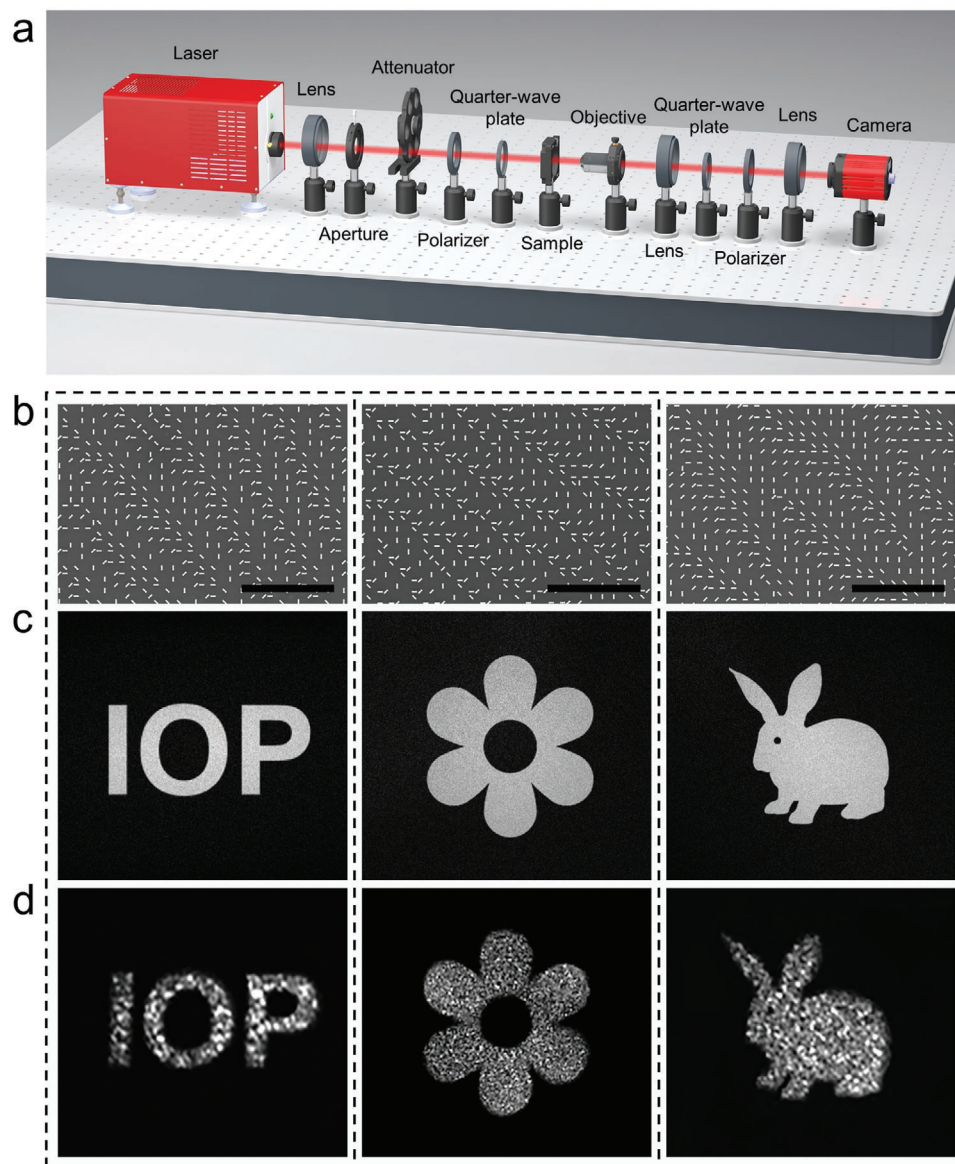


Figure 6. Experimental results of photonic routing of the metasurfaces. a) Schematic diagram of optical setup for photonic imaging measurement. The optical components are marked with corresponding labels. b) SEM images of the metasurface consisting of coded unit pixels for designated photonic routing. The scale bars are 10 μm . Numerical simulated c) and experimental d) results of photonic routing with different designed patterns at 1550 nm.

simulation results of the as-programmed metasurfaces are conducted using homemade algorithm and subsequently compared with the experimental results. In Figure 5c, three designated targets with different image configurations are displayed, where the bright areas represent the locations of light destinations. In addition, the related phase profiles and coding distributions are also provided.

Since only the nanofin units in amorphous state contribute to the modulation of wavefront, the programmed metasurface and the metasurface consisting only of amorphous nanofins should yield the same results. Thus, taking convenience into account, it is feasible to demonstrate the proposed photonic imaging by fabricating the metasurfaces with coded unit pixels. The fabricated samples are shown in Figure 6b, which also follow the

fabrication process depicted in Figure S9 (Supporting Information). To measure the images, a homemade optical setup is employed (Figure 6a). Figure 6c,d displays the numerically simulated and experimental results of the designated imaging for photonic routing, in which three different images are presented. The transmitted light is routed to the designated area and captured by the NIR camera, as shown in Figure 6d. The consistent content between the simulated and experimental images confirms the reliability and flexibility of the NIR photonic routing of the metasurfaces. For practical routing applications, the metasurfaces would distribute the transmitted NIR signal to desired PIC terminals for optical linking. Compared to optical fiber communication, this wireless optical connection method offers greater spatial modulation freedom and development potential, thereby

enlightening new directions for the future applications of metasurfaces.

Since the programming operation is expected to be implemented by pulsed laser, precise control of the laser beam is necessary to accurately irradiate the unit pixels. In addition, the phase transition behavior of GST is usually limited by its thickness due to the crystallization kinetics. Several parameters of pulsed laser (e.g., pulse energy, spot size, and exposure time) along with the focusing objective lens should be properly adjusted to achieve reversibly modulation of the thick GST structures.

4. Conclusion

In conclusion, we design and experimentally demonstrate an NIR bilayer metasurfaces with codable unit pixels for photonic routing. The unit pixel of the metasurfaces adopts a double-layer structure configuration with the upper GST nano-antenna and the underneath α -Si nanofin. The α -Si nanofins and GST nano-antennas contribute to cross-polarization generation and amplitude modulation of cross-polarization light, respectively. It is important that the all-dielectric structure design largely diminish the unnecessary transmission light loss compared with metallic counterpart. The optimal GST height is identified through parameter sweeping during the simulation process. The tunable metasurfaces with identical unit cell orientation are fabricated to verify the transmissivity modulation of the cross-polarization light. According to the measured result, the PCV induced by GST phase change is $\approx 55\%$ at around 1550 nm, demonstrating large modulation depth of PCE. On that basis, the metasurfaces constituted by arranged four-level phase unit pixels is proposed. Each unit pixel in the supercell can be independently coded, resulting in the breaking of the destructive interference balance and thus output of cross-polarized light with large intensity and desired PB phase delay. To verify the photonic routing ability of the proposed scheme, we fabricated the metasurfaces with coded unit pixels to realize photonic imaging. Compared with previous active metasurfaces for phase control which possess finite switchable states,^[44,45] the metasurfaces with four-level programmability allow much more controllable output channels, which greatly expand the active control scope and enhance the modulation degree of freedom. In addition, benefitting from the significant optical parameter contrast caused by the phase transition of GST and the unique bilayer structure configuration, the PCV in NIR region achieves an excellent level. Our results provide a universal template for NIR wavefront shaping, offering significant application potential for wireless routing communication. It is worth noting that metasurfaces with programmability for visible wavefront modulation are also attractive. Further efforts deserve to be made to achieve this goal by utilizing an improved metasurface structure which based on phase change materials (e.g., Sb_2S_3 , $\text{Ge}_2\text{Sb}_2\text{Se}_4$, Te). In addition, it is advisable to programming large-area metasurfaces with fast computation methods, such as ad-joint optimization^[46,47] and machine learning approaches.^[48]

5. Experimental Section

Numerical simulation: The optical transmission spectra and electric field profiles of the designed metasurfaces were simulated using the FDTD

method. The periodic boundary condition was adopted along both x and y in-plane directions and perfectly matched layers (PML) boundary condition was set along the propagation of electromagnetic waves (out-of-plane z direction). A uniform grid with a maximum mesh step of 10 nm along all directions was used to discretize the simulation region. Circularly polarized light was launched incident to the unit cell along z direction and the light was set to propagate forward. 2D frequency-domain monitors were set to record the needed data of electrical field. The refractive index and extinction coefficient of GST and α -Si used in the simulations were obtained through spectral ellipsometry measurements (see Figure 2b; Figure S1, Supporting Information). The phase distribution of photonic routing was calculated by Gerchberg–Saxton (GS) algorithm, and the detailed calculation processes were illustrated in Figure S11 (Supporting Information). The operation of GS algorithm, programming computation, and numerical simulation of imaging were obtained through MTALAB numerical computation.

Device Fabrication: The silicon dioxide plates with thickness of 500 nm were chosen as the substrate to support the upper nanostructures. Prior to fabrication, the substrates underwent ultrasonic cleaning in acetone, isopropanol, and ultrapure water, which were then dried using nitrogen flow. The devices were subsequently fabricated according to following steps. First, the 550 nm α -Si film was deposited on the substrate by inductively coupled plasma enhanced chemical vapor deposition (ICPECVD) at 130 °C, during which the gas flow rates of SiH_4 , H_2 , and Ar were 15, 65, and 250 sccm, respectively. The deposition pressure was kept at 11 mTorr with radio frequency (RF) power of 5 W and ICP power of 40 W. Then, the α -GST film with thickness of 250 nm was deposited by magnetron sputtering (MS) method at room temperature. The deposition process was performed using a synthesized single target with Ar gas flow rate at 10 sccm, chamber pressure at 7 mTorr, and sputtering RF power of 100 W. After that, the methyl methacrylate (MMA EL6) and polymethyl methacrylate (PMMA 495K) films of ≈ 150 nm and ≈ 300 nm were spin-coated in turn on the top of the α -GST film at 4000 rpm and 2000 rpm, respectively. For the sake of preventing GST phase change, the samples were baked at 95 °C for 15 min at the hotplate after each coating process. The double layers of photoresist with different irradiation sensitivities would form under-cut structures, which were convenient for lift-off process. Afterward, an electron beam lithography (EBL) process with an accelerating voltage of 100 kV, 2 nA beam current, and dosage of 1000 $\mu\text{C cm}^{-2}$ was employed to write the exposure pattern on the photoresist. The desired pattern was thus obtained after developing in a methyl isobutyl ketone/isopropyl alcohol (MIBK/IPA) mixture. Subsequently, the SiO_2 masks with 130 nm in thickness was deposited at 90 °C by electron beam evaporation (EBE) deposition, which was followed by a lift-off process to remove the unnecessary portion. Finally, inductively coupled plasma reactive ion etching (ICP-RIE) was performed using HBr gas at 20 °C with flow rate of 50 sccm, pressure of 4 mTorr, RF power of 80 W, and ICP power of 750 W. The respective etching rates of GST and α -Si were ≈ 600 nm min^{-1} and ≈ 150 nm min^{-1} , and the etching process involved multiple cycles of 1 min duration each, with 1 min cooldown breaks between cycles. The heating of the metasurface samples and GST films for GST crystallization is performed in an annealing furnace. The annealing process was conducted under Ar gas atmosphere at 200 °C for 10 min.

Characterization of Samples: The experimental transmission spectra were measured on a Fourier-transform infrared spectrometer (Vertex 80, Bruker) coupled to an optical microscope (Hyperion 2000) with a $\times 15$ objective lens and a numerical aperture of 0.4. A homemade aperture was inserted at a suitable location between the light source and the sample to ensure the perpendicular incidence of the irradiation. The transmission spectra of a blank quartz plate were served as the reference for transmissive signal collection of the samples. The SEM photographs were taken on Hitachi Regulus 8230 with an accelerating voltage of 25 kV and a beam current of 7 nA. The elementary compositions of the GST films were obtained through EDS (Ultim Max, Oxford) analysis. The roughness of the GST films is characterized by AFM (Dimension Edge, Bruker). The Raman spectra of both α -GST and c -GST film were measured by LabRAM HR Evolution with 532 nm laser. The XRD measurement was performed using a PAN-analytical X-ray diffractometer with $\text{Cu } K_\alpha$ radiation. The refractive index and

extinction coefficient of GST and a-Si were measured on a spectral ellipsometer (SE 850 DUUV). The measurement of the near-infrared hologram images was carried out on a homemade optical setup (see Figure 5a). A 1550 nm laser (LDM1550, Thorlabs) and a near-infrared InGaAs camera (C12741-03, Hamamatsu) were adopted as the light source and photonic imaging recorder, respectively.

Supporting Information

Supporting Information is available from the Wiley Online Library or from the author.

Acknowledgements

C.L. and S.D. contributed equally to this work. This work was supported by the National Natural Science Foundation of China (Grant No. 12074420, U21A20140, 61888102, and 61905274), the Beijing Municipal Science & Technology Commission, Administrative Commission of Zhongguancun Science Park (No. Z211100004821009), the Chinese Academy of Sciences through the Project for Young Scientists in Basic Research (YSBR-021), and the Key Research Program of Frontier Sciences of Chinese Academy of Sciences (Grant No. QYZDJ-SSWSLH042 and XDPB22). This work is also supported by the Synergic Extreme Condition User Facility, China.

Conflict of Interest

The authors declare no conflict of interest.

Data Availability Statement

The data that support the findings of this study are available from the corresponding author upon reasonable request.

Keywords

metasurfaces, phase change materials, photonic routing, tunable polarization conversion, wavefront modulation

Received: September 4, 2023
Revised: November 9, 2023
Published online:

- [1] J. M. Arrazola, V. Bergholm, K. Brádler, T. R. Bromley, M. J. Collins, I. Dhand, A. Fumagalli, T. Gerrits, A. Goussev, L. G. Helt, J. Hundal, T. Isacsson, R. B. Israel, J. Izaac, S. Jahangiri, R. Janik, N. Killoran, S. P. Kumar, J. Lavoie, A. E. Lita, D. H. Mahler, M. Menotti, B. Morrison, S. W. Nam, L. Neuhaus, H. Y. Qi, N. Quesada, A. Reppingon, K. K. Sabapathy, M. Schuld, et al., *Nature* **2021**, 591, 54.
- [2] Y. Shen, N. C. Harris, S. Skirlo, M. Prabhu, T. Baehr-Jones, M. Hochberg, X. Sun, S. Zhao, H. Larochelle, D. Englund, M. Soljacic, *Nat. Photonics* **2017**, 11, 441.
- [3] D. R. Solli, B. Jalali, *Nat. Photonics* **2015**, 9, 704.
- [4] S. Xu, J. Wang, S. Yi, W. Zou, *Nat. Commun.* **2022**, 13, 7970.
- [5] A. Alduino, M. Paniccia, *Nat. Photonics* **2007**, 1, 153.
- [6] R. Kirchain, L. Kimerling, *Nat. Photonics* **2007**, 1, 303.
- [7] A. W. Elshaari, W. Pernice, K. Srinivasan, O. Benson, V. Zwiller, *Nat. Photonics* **2020**, 14, 285.
- [8] N. F. Yu, P. Genevet, M. A. Kats, F. Aieta, J. P. Tetienne, F. Capasso, Z. Gaburro, *Science* **2011**, 334, 333.
- [9] G. Zheng, H. Mühlenbernd, M. Kenney, G. Li, T. Zentgraf, S. Zhang, *Nat. Nanotechnol.* **2015**, 10, 308.
- [10] C. Jung, G. Kim, M. Jeong, J. Jang, Z. Dong, T. Badloe, J. K. W. Yang, J. Rho, *Chem. Rev.* **2021**, 121, 13013.
- [11] D. Lin, P. Fan, E. Hasman, M. L. Brongersma, *Science* **2014**, 345, 298.
- [12] M. Khorasaninejad, W. T. Chen, R. C. Devlin, J. Oh, A. Y. Zhu, F. Capasso, *Science* **2016**, 352, 1190.
- [13] M. Khorasaninejad, F. Capasso, *Science* **2017**, 358, eaam8100.
- [14] S. Du, Z. Liu, C. Sun, W. Zhu, G. Geng, H. Ye, J. Li, C. Gu, *Nanophotonics* **2021**, 10, 1505.
- [15] F. Ding, Z. X. Wang, S. L. He, V. M. Shalaev, A. V. Kildishev, *ACS Nano* **2015**, 9, 4111.
- [16] S. Sun, K.-Y. Yang, C.-M. Wang, T.-K. Juan, W. T. Chen, C. Y. Liao, Q. He, S. Xiao, W.-T. Kung, G.-Y. Guo, L. Zhou, D. P. Tsai, *Nano Lett.* **2012**, 12, 6223.
- [17] X. Yin, T. Steinle, L. Huang, T. Taubner, M. Wuttig, T. Zentgraf, H. Giessen, *Light: Sci. Appl.* **2017**, 6, e17016.
- [18] Y. Zhang, C. Fowler, J. Liang, B. Azhar, M. Y. Shalaginov, S. Deckoff-Jones, S. An, J. B. Chou, C. M. Roberts, V. Liberman, M. Kang, C. Ríos, K. A. Richardson, C. Rivero-Baleine, T. Gu, H. Zhang, J. Hu, *Nat. Nanotechnol.* **2021**, 16, 661.
- [19] Y. Wang, P. Landreman, D. Schoen, K. Okabe, A. Marshall, U. Celano, H.-S. P. Wong, J. Park, M. L. Brongersma, *Nat. Nanotechnol.* **2021**, 16, 667.
- [20] Y. Kim, P. C. Wu, R. Sokhoyan, K. Mauser, R. Gludell, G. Kafaei Shirmanesh, H. A. Atwater, *Nano Lett.* **2019**, 19, 3961.
- [21] C. Zheng, R. E. Simpson, K. Tang, Y. Ke, A. Nemati, Q. Zhang, G. Hu, C. Lee, J. Teng, J. K. W. Yang, J. Wu, C.-W. Qiu, *Chem. Rev.* **2022**, 15450.
- [22] T. J. Cui, M. Q. Qi, X. Wan, J. Zhao, Q. Cheng, *Light: Sci. Appl.* **2014**, 3, e218.
- [23] X. G. Zhang, W. X. Jiang, H. L. Jiang, Q. Wang, H. W. Tian, L. Bai, Z. J. Luo, S. Sun, Y. Luo, C.-W. Qiu, T. J. Cui, *Nat. Electron.* **2020**, 3, 165.
- [24] J. Wu, Z. Shen, S. Ge, B. Chen, Z. Shen, T. Wang, C. Zhang, W. Hu, K. Fan, W. Padilla, Y. Lu, B. Jin, J. Chen, P. Wu, *Appl. Phys. Lett.* **2020**, 116, 131104.
- [25] L. Chen, Q. Ma, Q. F. Nie, Q. R. Hong, H. Y. Cui, Y. Ruan, T. J. Cui, *Photonics Res.* **2021**, 9, 116.
- [26] J. Park, B. G. Jeong, S. I. Kim, D. Lee, J. Kim, C. Shin, C. B. Lee, T. Otsuka, J. Kyoung, S. Kim, K.-Y. Yang, Y.-Y. Park, J. Lee, I. Hwang, J. Jang, S. H. Song, M. L. Brongersma, K. Ha, S.-W. Hwang, H. Choo, B. L. Choi, *Nat. Nanotechnol.* **2021**, 16, 69.
- [27] Z. R. Fang, R. Chen, J. E. Fröch, Q. A. Tanguy, A. I. Khan, X. J. Wu, V. Tara, A. Manna, D. Sharp, C. Munley, F. Miller, Y. Zhao, S. J. Geiger, K. F. Böhringer, M. Reynolds, E. Pop, A. Majumdar, (Preprint) arXiv:2307.12103, submitted: July **2023**.
- [28] M. Wuttig, N. Yamada, *Nat. Mater.* **2007**, 6, 824.
- [29] M. Wuttig, V. L. Deringer, X. Gonze, C. Bichara, J.-Y. Raty, *Adv. Mater.* **2018**, 30, 1803777.
- [30] T. H. Lee, S. R. Elliott, *Adv. Mater.* **2020**, 32, 2000340.
- [31] S. Abdollahramezani, O. Hemmatyar, M. Taghinejad, H. Taghinejad, A. Krasnok, A. A. Eftekhar, C. Teichrib, S. Deshmukh, M. A. El-Sayed, E. Pop, M. Wuttig, A. Alù, W. Cai, A. Adibi, *Nat. Commun.* **2022**, 13, 1696.
- [32] Y. Zhang, C. Fowler, J. Liang, B. Azhar, M. Y. Shalaginov, S. Deckoff-Jones, S. An, J. B. Chou, C. M. Roberts, V. Liberman, M. Kang, C. Ríos, K. A. Richardson, C. Rivero-Baleine, T. Gu, H. Zhang, J. Hu, *Nat. Nanotechnol.* **2021**, 16, 661.
- [33] Q. Wang, E. T. F. Rogers, B. Gholipour, C. M. Wang, G. H. Yuan, J. H. Teng, N. I. Zheludev, *Nat. Photonics* **2016**, 10, 60.
- [34] Z. R. Fang, R. Chen, J. J. Zheng, A. Majumdar, *IEEE J. Sel. Top. Quantum Electron.* **2022**, 28, 8200317.

- [35] S. Abdollahramezani, O. Hemmatyar, H. Taghinejad, A. Krasnok, Y. Kiarashinejad, M. Zandehshahvar, A. Alù, A. Adibi, *Nanophotonics* **2020**, *9*, 1189.
- [36] N. Youngblood, C. A. Ríos Ocampo, W. H. P. Pernice, H. Bhaskaran, *Nat. Photonics* **2023**, *17*, 561.
- [37] F. Aieta, P. Genevet, M. Kats, F. Capasso, *Opt. Express* **2013**, *21*, 31530.
- [38] M. Pan, Y. Fu, M. Zheng, H. Chen, Y. Zang, H. Duan, Q. Li, M. Qiu, Y. Hu, *Light: Sci. Appl.* **2022**, *11*, 195.
- [39] A. She, S. Zhang, S. Shian, D. R. Clarke, F. Capasso, *Opt. Express* **2018**, *26*, 1573.
- [40] Y. Zhang, J. B. Chou, J. Li, H. Li, Q. Du, A. Yadav, S. Zhou, M. Y. Shalaginov, Z. Fang, H. Zhong, C. Roberts, P. Robinson, B. Bohlin, C. Ríos, H. Lin, M. Kang, T. Gu, J. Warner, V. Liberman, K. Richardson, J. Hu, *Nat. Commun.* **2019**, *10*, 4279.
- [41] Y. Canvel, S. Lagrasta, C. Boixaderas, S. Barnola, Y. Mazel, E. Martinez, *J. Vac. Sci. Technol. A* **2019**, *37*, 031302.
- [42] T. D. Bestwick, G. S. Oehrlein, *J. Vac. Sci. Technol. A-Vac. Surf. Films* **1990**, *8*, 1696.
- [43] A. Leitis, A. Heßler, S. Wahl, M. Wuttig, T. Taubner, A. Tittl, H. Altug, *Adv. Funct. Mater.* **2020**, *30*, 1910259.
- [44] J. Li, S. Kamin, G. Zheng, F. Neubrech, S. Zhang, N. Liu, *Sci. Adv.* **2018**, *4*, eaar6768.
- [45] X. Liu, Q. Wang, X. Zhang, H. Li, Q. Xu, Y. Xu, X. Chen, S. Li, M. Liu, Z. Tian, C. Zhang, C. Zou, J. Han, W. Zhang, *Adv. Opt. Mater.* **2019**, *7*, 1900175.
- [46] M. Mansouree, A. Mcclung, S. Samudrala, A. Arbabi, *ACS Photonics* **2021**, *8*, 455.
- [47] M. Zhou, D. Liu, S. W. Belling, H. Cheng, M. A. Kats, S. Fan, M. L. Povinelli, Z. Yu, *ACS Photonics* **2021**, *8*, 2265.
- [48] L. Li, H. Ruan, C. Liu, Y. Li, Y. Shuang, A. Alù, C.-W. Qiu, T. J. Cui, *Nat. Commun.* **2019**, *10*, 1082.